# Facile 1D Graphene Fiber Synthesis from an Agricultural By-product: A Silicon-mediated Graphenization Route

Kazunori Fujisawa[1,2,*], Yu Lei[2,3], Carla de Tomas[4], Irene Suarez-Martinez[4], Chanjing Zhou[2,3], Yu-Chuan Lin[2,3], Shruti Subramanian[2,3], Ana Laura Elías[1,2], Masatsugu Fujishige[5], Kenji Takeuchi[5], Joshua A. Robinson[2,3], Nigel Anthony Marks[4], Morinobu Endo[5], Mauricio Terrones[1,2,3,5,6,**]

[1] Department of Physics, The Pennsylvania State University, University Park, Pennsylvania 16802, USA

[2] Center for 2-Dimensional and Layered Materials, The Pennsylvania State University, University Park, Pennsylvania 16802, USA

[3] Department of Materials Science and Engineering, The Pennsylvania State University, University Park, Pennsylvania 16802, USA

[4] Department of Physics and Astronomy, Curtin University, Perth WA 6845, Australia

[5] Institute of Carbon Science and Technology, Shinshu University, 4-17-1 Wakasato, Nagano 380-8553, Japan

[6] Department of Chemistry, The Pennsylvania State University, University Park, Pennsylvania 16802, USA

---

**\* Corresponding author:** Tel: +1-814-863-6774. E-mail: kuf15@psu.edu (Kazunori Fujisawa)

**\*\* Corresponding author:** Tel: +1-814 865-0343. E-mail: mut11@psu.edu (Mauricio Terrones)

**Abstract**

A one-dimensional (1D) graphene fiber with a novel structure has been prepared by a heat treatment of rice husk, a natural by-product that contains high amounts of silica. A step-by-step heat treatment of rice husk revealed that (i) carbonization yields porous carbon and silica, (ii) 1D $\beta$-SiC nanowires are formed by the carbothermic reduction of silica, (iii) finally 1D graphene fibers are created by silicon sublimation from 1D $\beta$-SiC nanowires. Raman spectroscopy and electron microscopy studies revealed that the graphene fiber is composed of a turbostratic multilayer structure. The SiC-derived material exhibits a large crystalline size and turbostratic stacking making each layer as quasi-free-standing graphene, which is confirmed by the 3.9 times higher Raman G'-band intensity over the G-band intensity. Molecular dynamics simulations revealed a high diffusion rate of Si atoms and a volume reduction of the SiC structure at the sublimation temperature. Since the silicon sublimation occurred from multiple points of the SiC nanowire, this led to radially-collapsed fibers and faceted structures with thick-graphitic-layer that are inter-connected (deflated-balloons and inter-connected balloon-like fibers). This facile synthesis route opens up a new avenue to the cost-effective and etching-free production of self-standing graphene for its bulk usage.

## 1. Introduction

Graphene is a one-atom-thick two dimensional (2D) material which was firstly isolated from its bulk form, graphite, in 2004 [1]. Owing to its excellent physico–chemical properties, such as high surface area, carrier mobility, transparency, mechanical strength, and thermal conductivity among others, graphene has attracted much attention in scientific and industrial research fields [2]. Several preparation methods for graphene have been established; (i) mechanical/liquid exfoliation [1,3], (ii) reduction of graphene oxide [4], (iii) chemical vapor deposition (CVD) [5,6] and (iv) decomposition of silicon carbide (SiC) [7,8]. Among these preparation methods, CVD has been extensively used to prepare large area graphene. However, the preparation of graphene by the CVD method still requires a metallic substrate (e.g. copper foil) as a catalyst for hydrocarbon dehydration, as well as a template for 2D growth. The dehydration of hydrocarbon is a surface reaction; thus the synthesis of graphene is limited by the area of the metallic substrate. On the other hand, another kind of nanocarbon—carbon nanotubes (CNTs)—has been synthesized using a catalytic CVD process where the growth of micron-sized CNTs are guided by nano-sized metal particle catalysts—as opposed to a large macroscopic metallic sheet—thus less metal catalyst is needed [9,10]. Moreover, since CVD-based graphene is not self-standing, the metal substrate has to be removed by a transfer process, which also limits the direct usage of graphene for several applications. Therefore, considering the bulk use of graphene, a cost-effective synthesis strategy for self-standing graphene that minimizes the amount of used metal is required.

Rice husk is known as a Si-rich natural by-product from rice harvest, as it contains 15–20%

of silica ($SiO_x$) at its outer shell [11,12]. Since the major elements within rice husk are carbon, silicon and oxygen, various silicon-based materials (Si [12–15], $SiO_2$ [16,17], SiC [18–20], $Si_3N_4$ [21–23]), carbon-based materials (hard carbon [24], activated carbon [25], graphene quantum dots [26], corrugated graphene [27], carbon nanotube-graphene hybrid [28]) and their composites [29], have been derived from it in the past. Moreover, bulk amounts of nanomaterials have been prepared using rice husk as a starting material. For example, Jung *et al.*, prepared a high purity 3D-porous Si from rice husk for lithium ion battery applications by acid-leaching and a magnesiothermic reduction [12]. Muramatsu *et al.*, reported the preparation of rice husk-based corrugated graphene structures for applications in electric double layer capacitors [27], and other types of morphologically-rich carbon materials have been produced using rice husk as a starting material. Although some carbon materials prepared from rice husk are called graphene according to previous reports, they do not have a linear Dirac-dispersion, which is an intrinsic property of graphene [1,30]. This might be due to the strong coupling between layers, small grain size and non-uniform structure of such rice husk-derived graphitic structures.

In this study, we performed the synthesis of novel one-dimensional (1D) structure of quasi freestanding graphene by heat-treating the agricultural by-product rice husk. A multi-step heat treatment was carried out to study the structural change occurring step-by-step. We observed that the 1D graphene structure was derived directly from 1D $\beta$-SiC nanowires. The transformation of rice husk into graphene fibers occurs as follows; (i) $SiO_2$ worked as a template for porous carbon generation from non-volatile organic components (such as, cellulose, lignin) in the rice husk structure; (ii) after raising the temperature to 1300 ºC,

gaseous SiO reacted with carbon to generate $\beta$-SiC nanowires, and (iii) finally, the high temperature driven silicon sublimation from the sacrificial 1D $\beta$-SiC template led to the formation of a 1D graphene structures. Raman spectroscopy revealed that the 1D graphene structure exhibited a G'-band over G-band intensity ratio of ~3.9, which indicates the presence of non-overlapped Dirac-cones. Transmission electron microscopy (TEM) studies showed a unique deflated-balloon and inter-connected balloon-like fibers. A molecular dynamics study revealed that a fast silicon diffusion at high temperatures leaves thin amorphous carbon on the SiC surface, which subsequently turns into the graphene structure. It has also been found that the fast silicon diffusion is responsible for the formation of this unique fiber morphology.

## 2. Experiment

### 2.1 Pretreatment and carbonization of rice husk by a low temperature heat treatment

Commercially available rice husk purchased from *Amazon.com* was used as the starting material (as-received-RH). Rice husk is a natural by-product, thus a non-uniform distribution of $SiO_x$, organic components (cellulose, lignin, *etc.*), and internal water content is expected. In order to increase the uniformity of the precursor, roughly 5 g of as-received-RH was milled in an inert liquid nitrogen (77K) environment (cryomilling, SPEX) for 45 min. An alumina ($Al_2O_3$) crucible filled with around 2.5 g of obtained fine ivory-colored powder of rice husk (raw-RH) was transferred to the inside of a quartz reaction tube. After purging the reaction tube with 600 sccm of Ar gas for 15 min, the temperature was increased while keeping the system under an inert Ar flow. The temperature ramp of the electric furnace was set to 10 °C

min$^{-1}$. Three dwell temperatures were used: 100 °C for 30 min, 600 °C for 30 min and 1100 °C for 30 min, in order to remove most heteroatoms, functional groups, and organic components. After the reaction, the furnace was cooled naturally and then, a black-colored powdery material was obtained (lowHT-RH).

## 2.2 Synthesis of *β*-SiC nanowires by a middle temperature heat treatment

A mixture of silicon carbide nanowires and a carbon structure was synthesized by heat-treating lowHT-RH at a further higher temperature (midHT-RH). An alumina (Al$_2$O$_3$) crucible filled with the resultant of the low temperature heat treatment (lowHT-RH) was placed inside an alumina (Al$_2$O$_3$) reaction tube. The treatment was carried out under a flow of 500 sccm of Ar. After purging the inside of the reaction tube with Ar gas for 15 min, the temperature was raised up to 1300 ºC using an electric furnace. The target temperature was maintained for 30 min.

## 2.3 Conversion of *β*-SiC nanowires to a 1D graphene fiber by a high temperature heat treatment

An additional step of high temperature heat treatment was performed on midHT-RH in order to obtain novel graphitic materials (highHT-RH). The high temperature heat treatment was carried out at 700 Torr of Ar atmosphere using an induction furnace (Graphite hot zone, Thermal Technologies LLC). A small portion of the *β*-SiC nanowires/carbon sample (midHT-RH) was contained in a graphite crucible to prevent oxidation by residual oxygen during the treatment. The temperature and dwell time of the heat treatment were 2000 °C and 2 h,

respectively.

## 2.4 Structure characterization

Thorough characterization of the raw materials and all the heat-treated samples was carried out. The surface morphology and elemental composition were revealed by scanning electron microscopy (SEM) and energy dispersive X-ray spectroscopy (EDS) analyses, using an FEI Nova NanoSEM630 field emission microscope. For raw-RH, the top surface was covered by a thin gold layer in order to reduce electric charging during observations. Further high magnification structural analysis was carried out using (scanning) transmission electron microscope (S/TEM). High-resolution TEM (HRTEM) images were acquired using a JEM-2010F (JEOL) and a Talos F200X (FEI), both operated at 200 kV. Talos F200X was also used for obtaining STEM images and for EDS analysis. An aberration corrected TEM study was carried out on a Titan$^3$ G2 60-300 (FEI) operated at 80 kV and with a monochromated electron beam. Raman spectra were acquired using an inVia Raman microscope (Rensihaw) equipped with a 514.5 nm laser. Back-scattered lights were collected through the same objective lens used for incident light, and an edge filter and a grating with 1800 l mm$^{-1}$ were used. Thermogravimetric analysis (TGA) was carried out in a Q5000 instrument (TA Instruments) under dry air flow (25 sccm) with a 10 $^o$C min$^{-1}$ of heating rate. Surface elemental analysis was carried out by X-ray photoelectron spectroscopy (XPS) using an Axis Ultra DLD (Shimadzu-Kratos) with a monochromated Al Kα X-ray source.

## 2.5 Molecular dynamics simulation

The heat treatment of a silicon carbide slab was simulated using the Molecular Dynamics LAMMPS package [31] and the Tersoff interatomic potential [32], used to describe the atomic interactions between Si–Si, Si–C and C–C atoms. The starting point of the simulation was a 1000-atom crystalline 3C-SiC (zinc blende) lattice of dimensions $2.1 \times 2.1 \times 2.1$ nm$^3$ in a simulation box of dimensions $42.1 \times 2.1 \times 2.1$ nm$^3$ with periodic boundary conditions in all dimensions. This set up allows the SiC lattice to have two free surfaces perpendicular to the x direction. The lattice was first equilibrated at room temperature for 10 ps. After equilibration, the lattice was annealed for 15 ns at 3600 K and a further 45 ns at a higher temperature of 4000 K to accelerate what is already a very slow process. These temperatures are below the SiC melting point in the Tersoff potential, which is around 4500 K [33]. Atoms evaporated from the surfaces were deleted when they were more than 3.5 nm away from the surface. Simulations were performed in the NVT ensemble with a timestep of 0.2 fs. Temperature control was achieved using the Bussi thermostat [34]. Diffusion coefficients were calculated from the slope of the mean-square displacement. Shortest-path rings statistic were computed using the Franzblau algorithm [35].

## 3. Results and discussion

Prior to heat treatment, as-received-RH was cryomilled at 77 K for 45 min to obtain a uniform fine powder of rice husk (raw-RH). The total amount of silica and any other ash content in raw-RH was determined to be 19.5 *wt.*% by TGA analysis under dry air (**Figure S1**). The weight loss at 100 °C indicated that raw-RH included ~10 *wt.*% of water content. The surface morphology of the raw-RH was characterized by SEM (**Figure 1(a)**) and EDS mappings

8

were acquired (**Figure S2**). After cryomilling, as-received-RH turned into a fine powder and, as revealed by the SEM-based EDS mapping, some impurities besides carbon, silicon, and oxygen, were found (**Table S1**).

### 3.1 Low temperature heat treatment: Carbonization

Carbonization is a process in which a carbon-containing precursor loses heteroatoms, functional groups or organic components, thus yielding carbon-rich materials. After the low temperature heat treatment of raw-RH, a black powder (lowHT-RH, **Figure 1(a) inset**) was obtained which mainly contains carbon and silica. The morphology of the obtained sample was investigated by SEM, and no obvious morphology change was observed after the low temperature heat treatment (**Figure 1(a) and (b)**). The amount of ash in the sample increased from 19.5 to 49.1 *wt.*% after the low temperature heat treatment (**Figure S1**), due to the removal of heteroatoms, functional groups, and volatile organic components. The crystalline structure characterization of obtained carbon/silica complex was examined by Raman spectroscopy (**Figure 1(c)**). There are two prominent peaks at 1350 cm$^{-1}$ and 1580 cm$^{-1}$ in $sp^2$-based carbon material's Raman spectra, which correspond to the disorder related D-band and the graphitic structure related G-band, respectively. The D-band is only activated when defects are present in the structure, thus the Raman intensity ratio of D-band over G-band ($I(D)/I(G)$) indicates the degree of disorder/defects in $sp^2$-based carbon structures. Since the carbonization temperature is not enough to remove all functional groups bonded to the surface of carbon structure, and lateral crystalline size is small and the intensity of D-band is close to that of G-band, which results in a ~1 $I(D)/I(G)$ ratio. A small shoulder is present at

the lower Raman shift tail of the D-band, at around 1100 cm$^{-1}$, which can be correlated to the polycyclic aromatic hydrocarbon (PAH)-like $sp^2$ structure with a finite size [36]. Both, the Raman spectrum and $I(D)/I(G)$ ratio did not change after removing silica by a chemical etching using diluted hydrofluoric acid (HF). In order to reveal details of the microstructure, the obtained material was investigated by TEM. **Figure 2(a)** exhibits a representative TEM image of the lowHT-RT sample. A few–50 nm-sized particles and surrounding relatively low crystalline materials were identified in the TEM images. Since the higher contrast is observed on the particles, these particle structures correspond to silica (**Figure 2(a) inset**). In order to confirm this point, elemental analysis was carried out by EDS (**Figure 2(b)**). The spatially resolved EDS signal shows a highly segregated distribution of silicon and carbon elements. The oxygen peak was found at the same location as silicon, which indicates the presence of silica. On the other hand, the only carbon signal was found on the surrounding structure. Details of the carbon structure were further characterized by inspecting the HF-treated lowHT-RH sample using HRTEM. After dissolving silica, a porous and corrugated carbon structure is revealed (**Figure 2(c)**). The EDS analysis shows that HF-treated lowHT-RH has a 99.7 *at.*% of carbon content (**Figure 2(d)**). Regarding TEM and EDS, it can be concluded that lowHT-RH is composed of nano-sized silica particles and a surrounding corrugate carbon structure, and that low crystalline carbon structure, is developed using silica as the template. A curved layer structure with short periodicity of corrugated carbon agrees with the high $I(D)/I(G)$ ratio resulted from the Raman analysis.
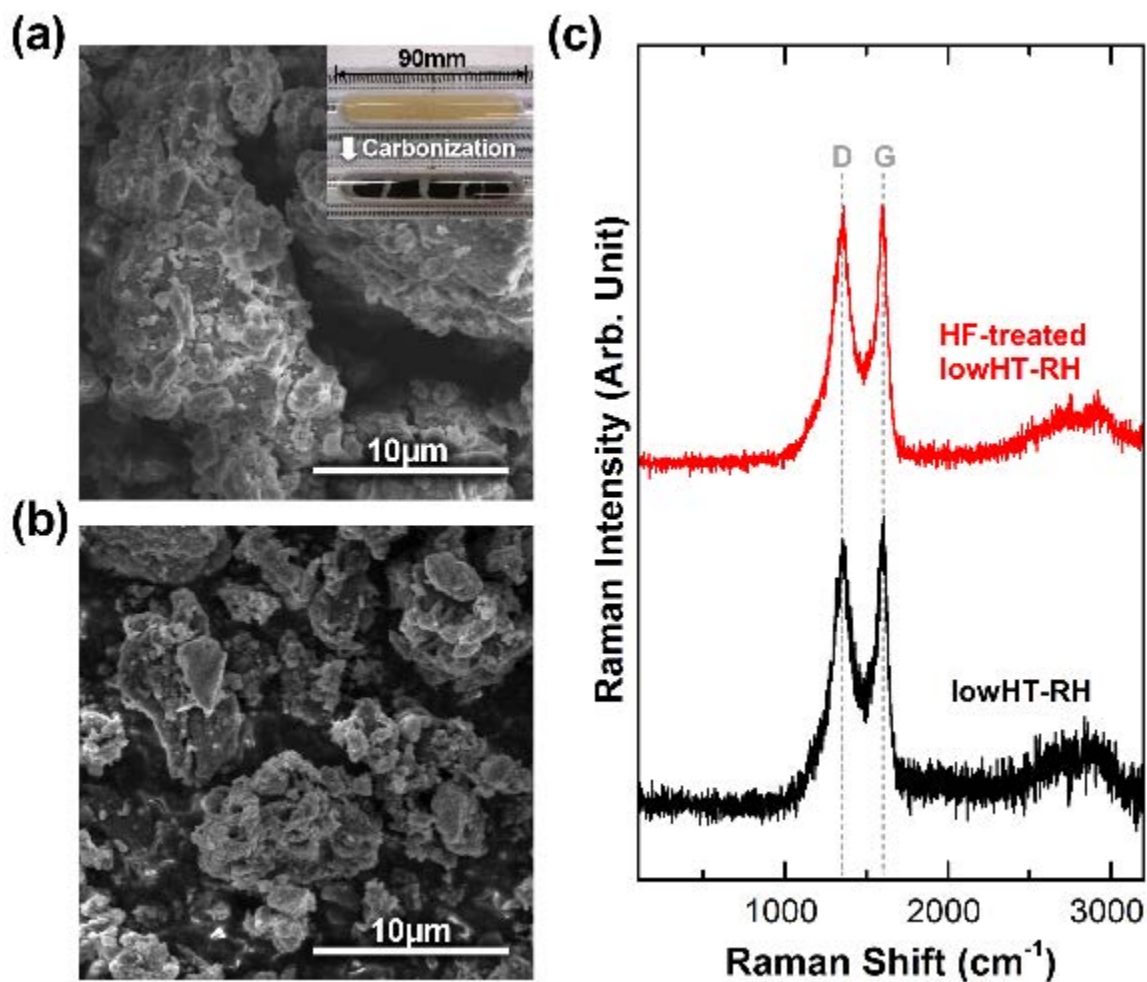
**Figure 1. (a–b)** SEM images of rice husk before (**(a)**, raw-RH) and after (**(b)**, lowHT-RH) low temperature heat treatment. The inset of (**a**) is an optical image of rice husk before and after low temperature heat treatment. **(c)**, Raman spectra of lowHT-RT excited by 514.5 nm. The Raman spectra did not change after the removal of $SiO_x$ template by HF.
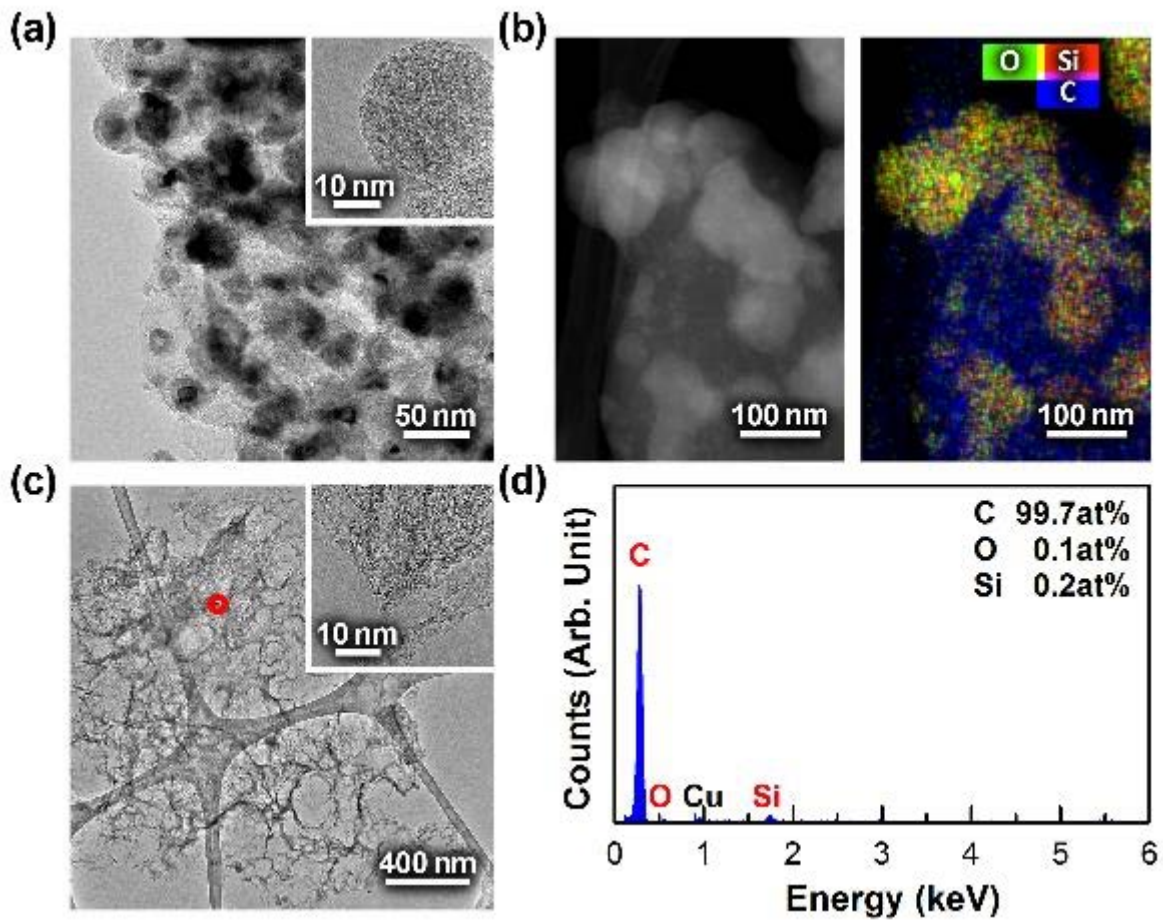
**Figure 2. (a)** HRTEM images of lowHT-RH. **(b)** STEM-HAADF image (left) and EDS elemental mapping (right) acquired at same area, which showing presence of segregated carbon and $SiO_x$ component. **(c)** HRTEM image of lowHT-RH after HF treatment. **(d)** Energy dispersed X-ray spectrum acquired from the marked area in **(c)**.
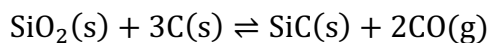
## 3.2 Middle temperature heat treatment: Carbothermic reduction

As a second step, the obtained silica and corrugated carbon complex was subjected to a second heat treatment at a higher temperature of 1300 °C (midHT-RH). After this middle temperature heat treatment, the outer surface of the powder sample turned grayish and whitish, as opposed to a completely black color before the heat treatment (**Figure 3(a) inset**). The surface morphology of the obtained material was initially investigated by SEM. At the grayish part of the midHT-RH sample (**Figure 3(a)**), mainly aggregate particles and a fibrous material were observed. SEM observations revealed that the whitish part was composed by a relatively high amount of fibrous material (**Figure 3(b)**). In order to investigate the crystalline structure of the material obtained at 1300 °C, Raman spectroscopy was employed (**Figure 3(c)**). Three differently colored parts were selected for Raman measurements. The black-part of the midHT-RH sample displays a Raman spectrum similar to the one corresponding to lowHT-RH, which indicates the presence of a low crystalline $sp^2$ hybridized carbon structure. Since the sample was later heat-treated at a higher temperature, narrower G- and D-bands are observed when compared to the lowHT-RH sample, which indicates a longer phonon life time due to the improvement of the lateral crystalline size of the $sp^2$ hybridized carbon structure. However, the $I(D)/I(G)$ ratio increased to values greater than 1, as the heat treatment temperature increased. The evolution of the D-band upon introduction of defects into the $sp^2$-hybridized carbon structures, can be categorized into two stages. The maximum $I(D)/I(G)$ ratio has been found at the transition between two stages whereas the peak width of the G- and D-band, continuously increases as defectiveness increases, thus an increase in $I(D)/I(G)$ together with the narrowing of bands corresponds to an increase in the

sample's degree of crystallinity [37,38]. When the gray- or white-colored part were examined by Raman spectroscopy, in addition to the $sp^2$ carbon components, another vibrational mode located at ~785 cm$^{-1}$ was observed, which matches to the transverse optical (TO) mode of the $\beta$-SiC (3C, zinc blende) structure [39]. In order to investigate the chemical bonding environment of midHT-RH, X-ray photoelectron spectroscopy was carried out (Figure S3(a)-(c)). There are only C, Si, O in the midHT-RH sample, and Si-C, Si-O-C, and Si-O were found for Si 2p region. The presence of the Si-O-C bond indicates subsequent surface oxidation of the $\beta$-SiC nanowires after the reaction. The observed Si-O bond is attributed to the surface oxide layer of the $\beta$-SiC nanowire and remaining $SiO_2$. At this temperature range (>1250 $^{\circ}$C), solid $SiO_2$ tends to react with solid carbon to generate gaseous SiO, followed by the formation of $\beta$-SiC nanowires.

$$SiO_2(s) + C(s) \rightleftharpoons SiO(g) + CO(g)$$

$$SiO(g) + 2C(s) \rightleftharpoons SiC(s) + CO(g)$$
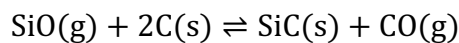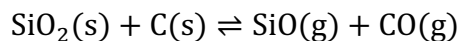
Moreover, a solid–solid reaction can also be proposed:

$$SiO_2(s) + 3C(s) \rightleftharpoons SiC(s) + 2CO(g)$$

However, in our case, $\beta$-SiC nanowires are only observed at the surface of lowHT-RH, thus this reaction should not be playing a major role upon $\beta$-SiC nanowires formation. The generated CO gas may react with $SiO_2$ particles to form $CO_2$. Subsequently, $CO_2$ may react with carbon to regenerate CO again, as follows:

$$CO_2(g) + C(s) \rightleftharpoons 2CO(g).$$
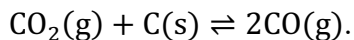
This carbothermic reduction of silica and the formation of $\beta$-SiC has been well known for several decades [20,40]. The structural detail of midHT-RH was investigated by S/TEM. The

TEM micrograph in **Figure 4(a)** depicts the $\beta$-SiC nanowire rich region of the sample. The non-uniform contrast over the $\beta$-SiC nanowire structures indicates the presence of stacking faults along the fiber's direction [39]. The measured distance within planes (0.250 nm) in the magnified image (**Figure 4(a) inset**), corresponds to the $\beta$-SiC (111) plane, and it can be concluded that the fiber was grown along the [111] direction. Several non-straight $\beta$-SiC nanowire structures, such as kinks and branches, have also been observed. Besides $\beta$-SiC nanowires, a corrugated carbon structure was found (**Figure 4(b)**). It is obvious that the crystallinity increases when midHT-RH is compared with lowHT-RH, and a similar corrugated carbon structure has been reported by Muramatsu *et al.* [27]. One of the possible mechanism for the realization of 1D growth of $\beta$-SiC is the vapor–liquid–solid (VLS) route [41]. As the rice husk contains some metal impurities (see **Figure S2 and Table S1**), such impurities can work as the catalyst for the growth of SiC fibers [42,43], as it occurs in the metallic nanoparticle-mediated CNT growth [9,10]. A small Fe particle at the tip of a $\beta$-SiC nanowire is depicted in **Figure 4(c)**. The presence of Fe particles located at the tip of $\beta$-SiC nanowires indicates that the VLS mechanism is responsible for the 1D growth of $\beta$-SiC [41,42]. In this mechanism, a vapor of SiO, CO or $CO_2$ that reaches the surface of an Fe particle dissolves into the particle, followed by the precipitation of a $\beta$-SiC nanowire from the supersaturated Fe particle, thus the Fe particle remains at the tip of the grown SiC nanowire [42]. In addition to the gaseous carbon precursor, solid carbons are also soluble into Fe particles. However, since the starting material exhibits a complicated structure and composition, several mechanisms, such as catalyst-free solid–vapor and solid–solid mechanism, could be behind the SiC nanowire growth [39].
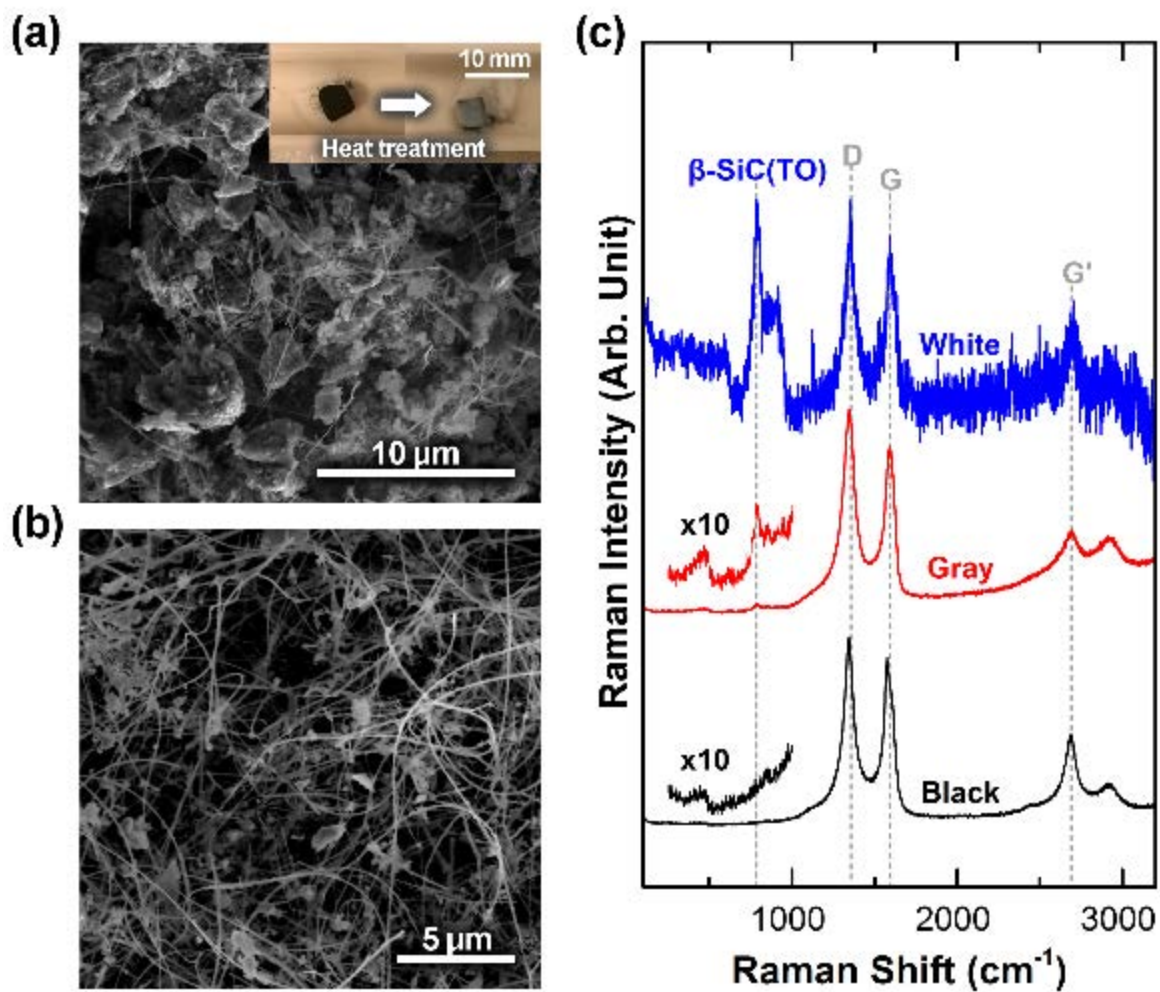
**Figure 3. (a–b)** SEM images of midHT-RH with gray-colored part **(a)** and with white-colored part **(b)**. The inset of **(a)** is an optical image of sample before and after middle temperature heat treatment. **(c)** Raman spectra of midHT-RT excited by 514.5 nm.
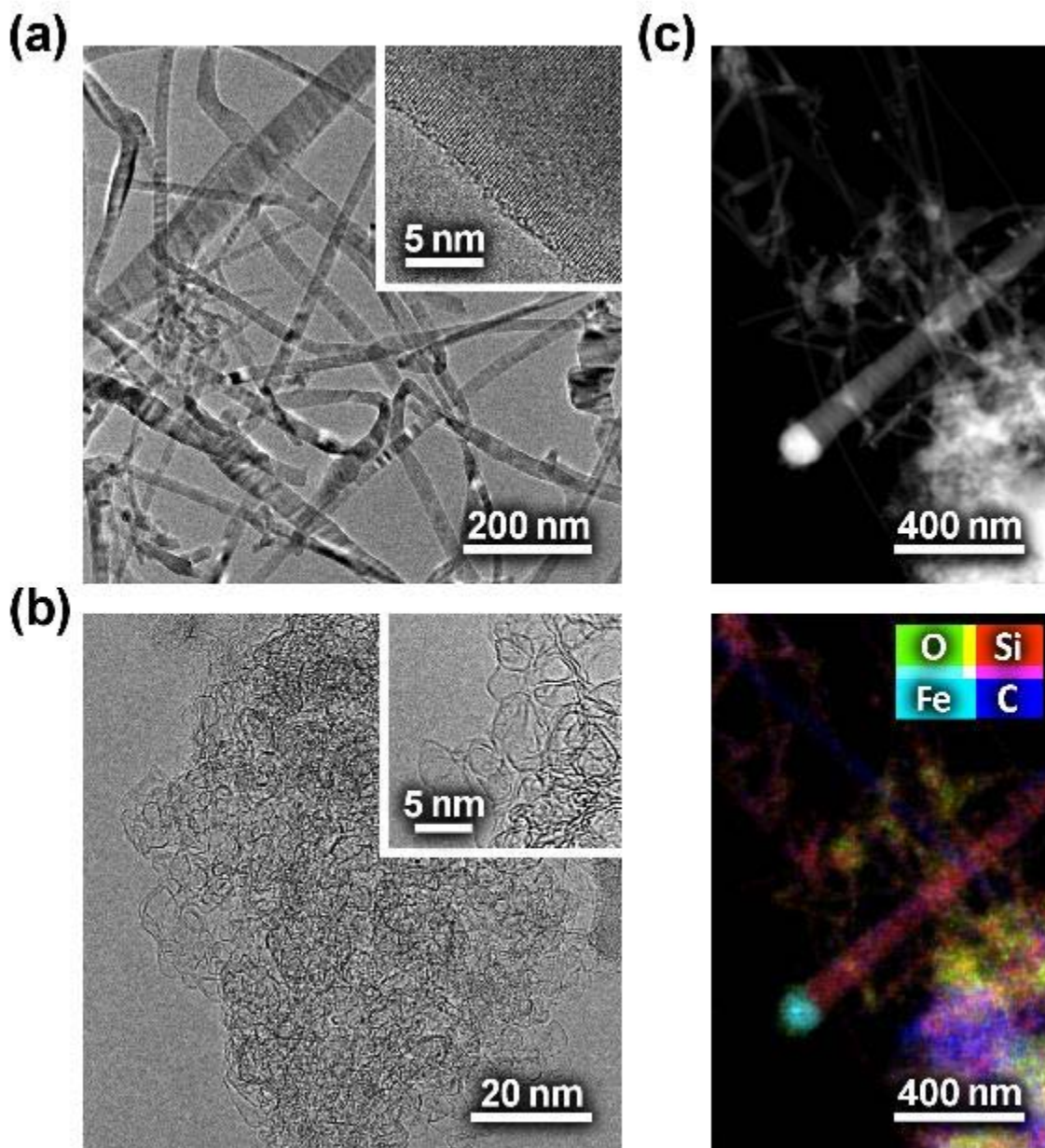
**Figure 4. (a–b)** HRTEM images of midHT-RH acquired from $\beta$-SiC nanowire part **(a)** and corrugated carbon part **(b)**. **(c)** STEM-HAADF image (top) and EDS elemental mapping (bottom) acquired at same area, which shows the presence of Fe nanoparticle at the tip of $\beta$-SiC nanowire.

### 3.3 High temperature heat treatment: Sublimation of Si and Graphene formation

A third and final heat treatment at the highest temperature was carried out on midHT-RH (β-SiC nanowire and carbon structure) at 2000 °C (highHT-RH). At such high temperatures, Si atoms sublimate from SiC structures. Therefore, such heat treatment yielded epitaxial graphene by the sublimation of Si from SiC [7,8]. After the high temperature heat-treatment, the sample turns black again (**Figure 5(a) inset**). When the surface morphology of highHT-RH was investigated by SEM, remaining 1D fibrous structures, which are highlighted by arrows in **Figure 5(a)** were found, in addition to particle structures. High resolution SEM analysis of the fiber-rich regions of highHT-RH revealed the presence of collapsed pockets that are often interconnected with each other, resembling a connected-balloon (**Figure 5(b) left and center**) and deflated-balloon structure (**Figure 5(b) right**). Again, the structural details of highHT-RH were investigated by Raman spectroscopy. From the acquired spectra, two distinguishable types of Raman signals were observed at the particle- and fiber-rich regions of the sample. The Raman spectra corresponding to the particle region are similar to that of a high temperature graphitized carbon material (**Figure 5(c)**, black-spectra) [44], whereas a graphene-like intense G'-peak (maximum $I(G')/I(G)$ is ~3.9) is observed at the fiber-like regions of highHT-RH (**Figure 5(c)**, red-spectra). Such intense G'-band ($I(G')/I(G) > 2$) has commonly been seen in monolayer graphene. This feature originates from the inter-band double resonance process at non-overlapped Dirac-cones [45]. When one more layer of graphene is stacked on top of a monolayer graphene sheet forming a bilayer graphene with a Bernal stacking, the G'-band splits into four bands due to the overlapping of Dirac-cones, causing the reduction of the $I(G')/I(G)$ ratio to ~1, along with the widening of

19

the G'-band. In the case of bilayer and multilayer graphene with non-Bernal (turbostratic) stacking, the G'-band remains similar to that of monolayer in terms of intensity, but shifts towards a higher Raman shift direction [46–49]. The observed high $I$(G')/$I$(G) indicates that the fiber-like regions of highHT-RH either are composed of monolayer graphene or a multilayer structure with turbostratic stacking. When the spectrum from the synthesized highHT-RH is compared with mechanically exfoliated graphene or CVD graphene, an observed blue shift of the G'-band supports the turbostratic stacking scenario (**Figure S4**). Besides the $I$(G')/$I$(G), other Raman peaks also provide more information about the number of layers and its stacking. The appearance of ZO'/ZA modes (~100 cm$^{-1}$) activated by the superlattice formation of rotated graphene layers [50,51], along with the absence of the M-band (1700–1800 cm$^{-1}$), and the peak positions/ratios of combination modes (iTALO$^+$/iTALO$^-$, iTOLA/LOLA, 1800–2100 cm$^{-1}$) [46,47], also indicate that the fiber-like region of highHT-RH contains multilayer graphene with a turbostratic (non-Bernal) stacking, rather than monolayer graphene (see **Figure S5**). The Raman behavior is similar to that of turbostratic bilayer graphene, where both top and bottom graphene sheets are highly decoupled, and thus behaves as quasi-free-standing graphene due to the preserved linear Dirac-dispersion [51,52]. In contrast to the fiber rich regions, the spectra acquired from the particle-like regions of highHT-RH exhibit the regular behavior of carbon material that has been graphitized at 2000 ºC, with a comparable intensity of G'- and G-bands. According to reported graphitization studies over various types of carbon materials, it can be concluded that a temperature of 2000 ºC is not enough to develop 3-dimensional ordering [44,53–55]. Therefore, carbon samples heat treated at ~2000 ºC show a similar behavior to that of the

particle-like region of highHT-RH, where the $I$(G')/$I$(G) ratio is close to 1 [44,54]. HRTEM images from the particle region of highHT-RH (**Figure 6(a)-(b)**) revealed the presence of aggregated multilayer graphitic structures. When comparing the obtained structure before (**Figure 4(b)**) and after (**Figure 6(a)**) the high-temperature heat treatment, it can be concluded that the corrugated monolayer structure was transformed into a multilayered structure. The magnified HRTEM image (**Figure 6(b)**) of the particle region shows a moiré pattern, and multiple hexagonal spots can be observed in the obtained fast Fourier transform (FFT) pattern (see **Figure 6(b) inset**). These features directly prove the presence of turbostratic stacking in the particle rich region of highHT-RH. This behavior is consistent with the graphitization behavior of carbon samples prepared at ~2000 °C, as previously mentioned. At the fiber-like regions of highHT-RH, carbon nanostructures with radially-collapsed fiber morphology (deflated-balloon structure) were observed (**Figure 6(c)**). The images shown in **Figure 6(d)** were acquired under STEM-HAADF (high-angle annular dark field) conditions. In this imaging mode, the ADF intensity changes with the atomic number ($Z$). According to the XPS results (**Figure S6**), less than 1 $at.$% of residual Si is still present in the highHT-RH sample, thus the observed contrast in the STEM-HAADF image is caused by a higher number of carbon atoms in the z-direction (thickness) rather than an elemental difference, if we ignore the effect of stacking. On the left and the center panels of **Figure 6(d)**, a bright line appears at the center of the fiber, which corresponds to a ripple. There are two graphitization pathways for midHT-RH sample: i) direct graphitization of amorphous carbon derived from the non-volatile components in rice husk, and ii) silicon-sublimation mediated graphitization of SiC. For the first case, the lateral size of the crystal is determined

by the orientation of the basic structural unit (BSU). Since the BSUs are randomly oriented in hard carbons, such as cellulose- and lignin-derived carbons, both the corrugated monolayer and the aggregated multilayer particle structures are formed at a low and high temperature, respectively. Upon high temperature heat treatment, the lateral crystalline size is enlarged by the effect of thermal energy. However, randomly oriented BSUs limit the crystalline size. In the second proposed pathway, which is SiC-derived graphitization, the carbon is generated at high temperature by silicon sublimation. When single crystal SiC is used for the preparation of epitaxial graphene, a continuous graphene structure beyond the step-edge has been observed in various types of SiC (4H, 6H [56], and 3C [57]) substrates. As depicted in **Figure 4(a)**, the $\beta$-SiC nanowire surface is flat, and the formation of the graphitic structure occurred epitaxially at high temperature through the sublimation of silicon, thus a large lateral size crystal is formed along the $\beta$-SiC nanowire structures. A turbostratic stacking has been found in SiC-derived graphene, which makes each graphene layer in turbostratic structure quasi-free-standing [52]. In this way, the lateral crystal size is not limited by the BSUs, thus graphenization is occurred before the development of 3-dimentional ordering of the layers (the final step of graphitization).
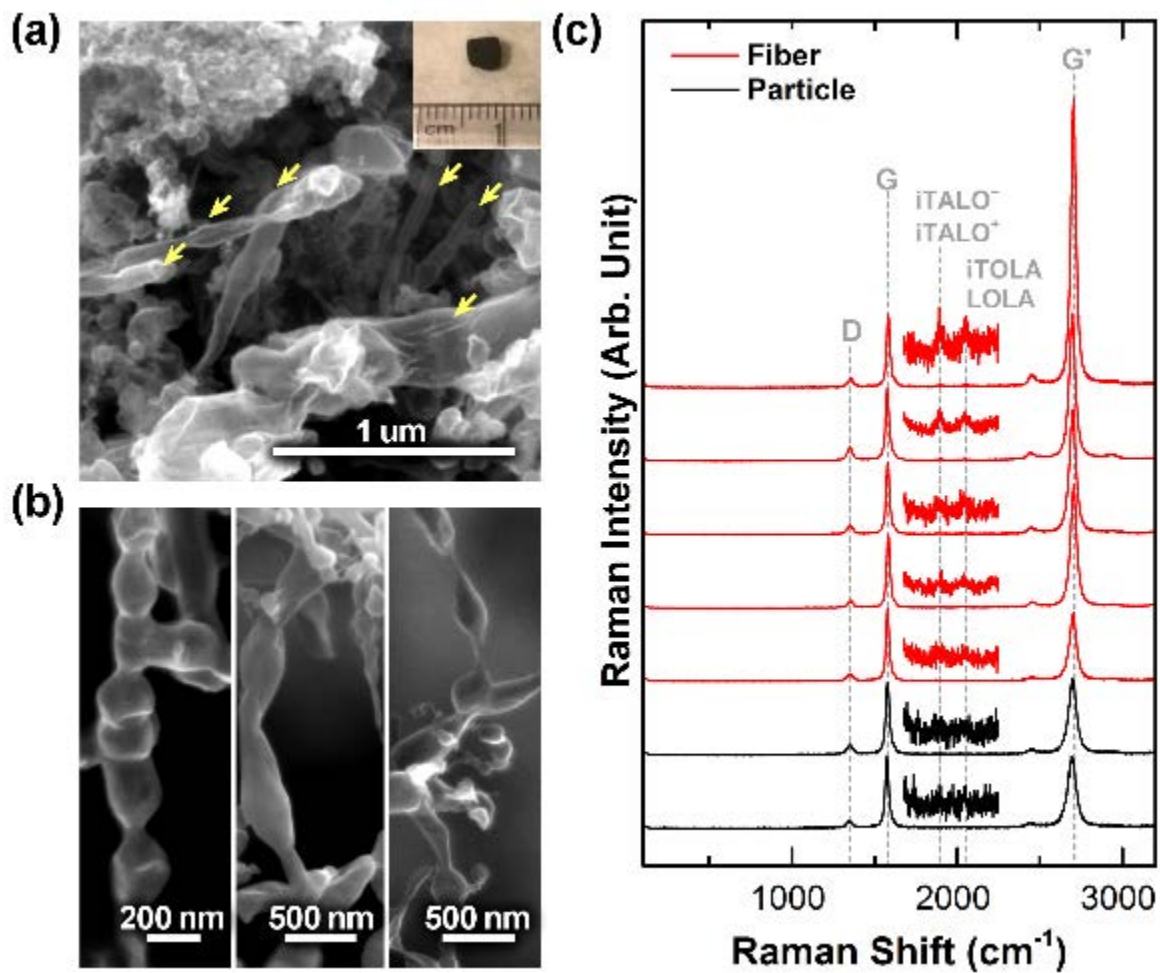
**Figure 5. (a)** SEM image of highHT-RH, arrows are highlighting fiber structure. **(b)** Magnified SEM images of various fiber structure. **(c)** Raman spectra of highHT-RH sample excited by 514.5 nm. The red- and black- colored spectra were obtained from the fiber part and the particle part, respectively.
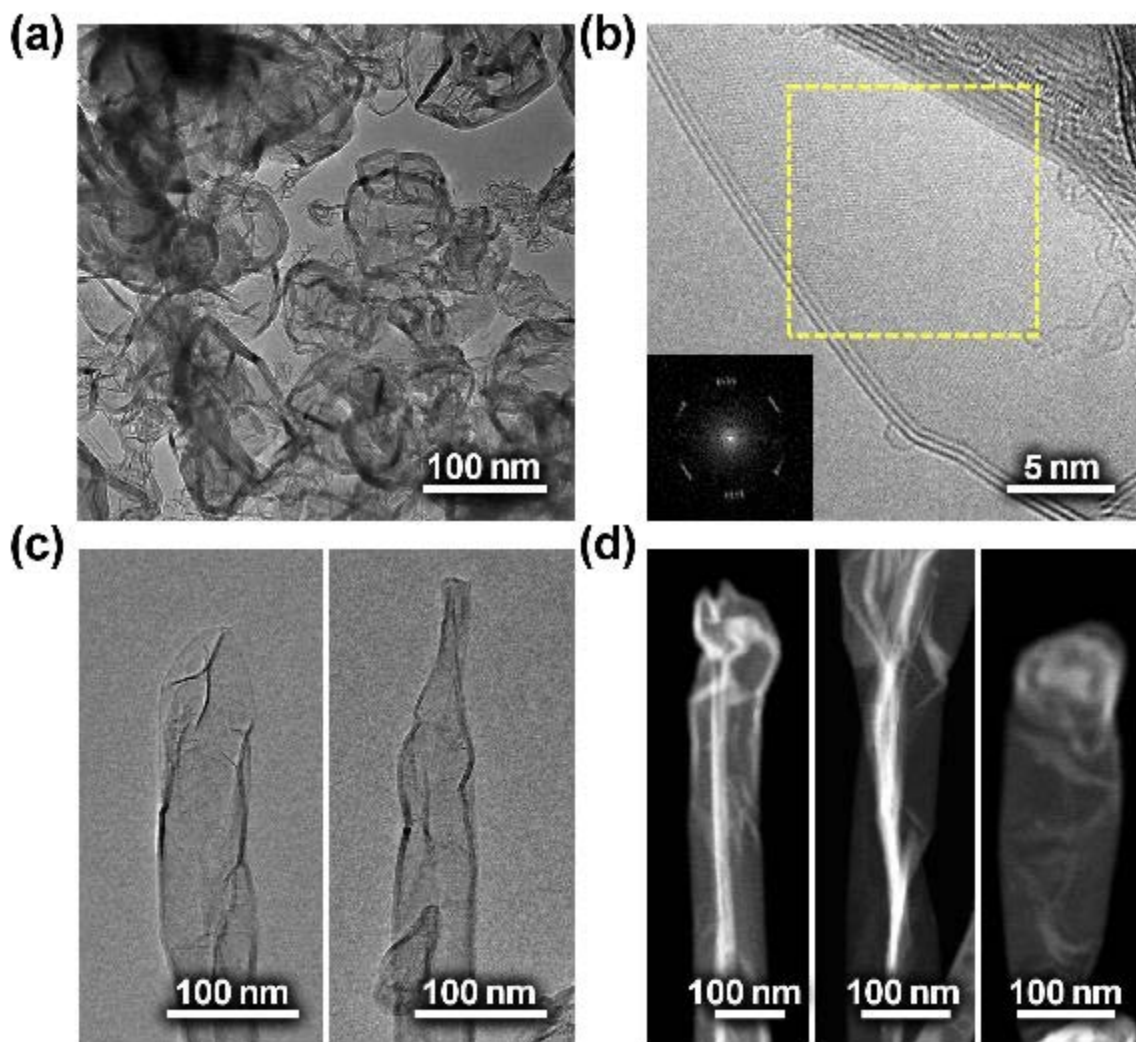
**Figure 6. (a–b)** Low-magnification **(a)** and high magnification **(b)** HRTEM images of highHT-RH with particle morphology. The inset of **(b)** corresponds to high-resolution fast Fourier transform patter acquired from rectangular area. **(c–d)** HRTEM **(c)** and STEM-HAADF **(d)** images of $\beta$-SiC-derived graphene fiber.

We have performed molecular dynamics simulations to interpret the last stage of the experiments where graphenization is observed upon high temperature heat treatment of $\beta$-SiC nanowires. To mimic the experiments we heat-treated a 3C-SiC crystalline lattice at a temperature approaching the SiC melting point. Upon heat treatment, we observe that the crystalline lattice becomes rapidly amorphous and Si atoms start to evaporate from the free surfaces at a much faster rate than carbon atoms. When most of the silicon is ejected, the amorphous carbon skeleton starts to graphitize into graphene-like layers. The entire process is illustrated visually in **Figure 7(a)** and quantified numerically in **Figure 7(b)-(c)**. The snapshots in **Figure 7(a)** show how the crystalline SiC structure evolves at high temperatures. The free surfaces on the left and right sides of the structure are the starting point for a disordering process, which proceeds inwards towards the center. At $t = 0.1$ ns, the structure appears fully amorphous. Shortly afterwards ($t = 0.2$ ns), the first Si atom evaporates from the surface and it is removed from the simulation. Over time (see **Figure 7(b)**, left axis), a large number of silicon atoms evaporate from the surface while very few carbon atoms evaporate. Indeed, by the time the first carbon atom evaporates at $t = 20$ ns, around 25% of the Si atoms have gone. At $t = 30$ ns half of the Si has evaporated and the carbon atoms begin to arrange into hexagons, the fundamental unit of graphene. By computing ring statistics, we convert the number of hexagons into an equivalent graphenization percentage, as shown on the right-axis of **Figure 7(b)**. The degree of graphenization was calculated from the number of hexagons per atom using the value of 0.5 hexagons per atom in ideal graphene as a reference. At $t = 50$ ns around 80% of the Si is gone and the carbon skeleton starts to graphitize significantly as shown in **Figure 7(b)**. At $t = 60$ ns, the carbon skeleton has

graphitized into defective graphene layers, which are stacked parallel to the evaporation surfaces. The right-most layer (shown in-plan view in the right-most panel) consists almost entirely of carbon hexagons with a few silicon impurities. The entire structure contains around 10% Si at this point, serving mainly to crosslink the other graphene-like layers. The simulation is then terminated, as the absence of van der Waals attractions in the Tersoff potential would prevent the graphene layers from sticking together.
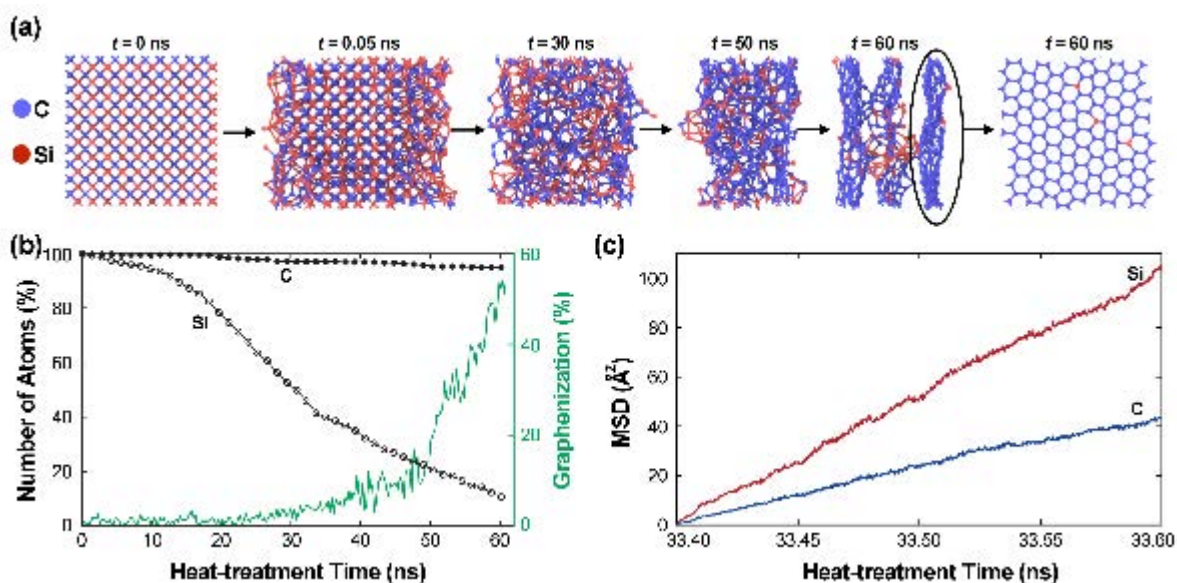


**Figure 7. (a)** Sequence of snapshots showing the time evolution of the SiC structure under heat treatment; carbon and silicon are colored in blue and red, respectively. Left to right; the initial SiC lattice ($t = 0$ ns); onset of amorphization ($t = 0.05$ ns); amorphous structure where half of the Si has evaporated ($t = 30$ ns); carbon skeleton with small amount of Si ($t = 50$ ns); graphitized carbon skeleton containing residual amounts of Si ($t = 60$ ns); plan view of the indicated graphene layer in panel ($t = 60$ ns). **(b)** Left axis: Number of carbon atoms (black circles) and silicon atoms (black open circles) remaining in the structure during the heat treatment time. Right axis: Evolution of the number of carbon hexagons (green solid line) with heat-treatment time. **(c)** Mean-square displacement (MSD) of carbon (blue) and silicon (red) with heat treatment time.

The main conclusion, however, is clear; namely that the Si fraction tends to zero, while the fraction of graphene-like bonding continually increases. An insight into why the Si atoms evaporate while the carbons do not is provided by **Figure 7(c)**, which plots the mean-square-displacement (MSD) at around $t = 33$ ns. The slope of the MSD corresponds to the diffusion coefficient, revealing that Si atoms diffuse with a mobility roughly 2.5 times that of carbon. The different behavior of carbon and silicon atoms can be explained based on the melting point of their pure forms. The melting point of pure silicon using the Tersoff potential is around 2700 K, while it is around 6000 K for carbon [32,33]. Therefore, heat-treating the SiC structure at 4000 K would provide sufficient energy to lose the crystalline structure, as Si atoms reach the free surface and evaporate, melting the Si phase. This observation corresponds exactly to the experimental situation where the high-temperature heat treatment is carried out at 2000 °C, which is above the experimental melting point of Si (1414 °C), yet below the melting point of SiC (2730 °C). Our simulations revealed the fast diffusion of Si atoms, as well as volume reduction of the SiC upon silicon-sublimation. Remaining SiC particles can also be observed at certain locations inside the fiber after the high temperature heat treatment has been conducted (**Figure S7**), indicating that silicon sublimation happened at multiple points of SiC nanowire structure. At the vicinity of the initiation point of silicon sublimation, a flat fiber structure with thin-layer is formed, and then radially-collapsed by the assistance of the negative pressure generated by the fast silicon diffusion inside the fiber (deflated-balloon structure). As the sublimation goes, SiC wire structure changed to particle structure, then a spherical structure with thick-graphitic-layer formed along the surface of the SiC particles inside the graphene fiber (inter-connected balloon-like structure).

## 4. Conclusion

The preparation of a self-standing graphene fiber was achieved through a facile heat treatment of rice husk, a natural byproduct. The rice husk is composed of $SiO_x$, which works as both a reactant and sacrificial template at different temperatures to produce carbon materials and carbides. Upon the temperature increase, porous carbon materials, silicon carbide nanowires and graphene fibers have been obtained via carbonization, carbothermic reduction, and graphenization processes, respectively. At the highest temperature the heat treatment was performed at, a fibrous carbon structure was observed, together with a particle-like carbon structure. Detailed Raman and S/TEM analyses showed that the fiber is composed by highly decoupled graphene, which exhibits a ~3.9 $I(G')/I(G)$ ratio whereas the particle-like region shows an expected carbon graphitization behavior ($I(G')/I(G) \sim 1$). The highly crystalline carbon layered material produced can be considered quasi-free-standing graphene. The large, crystalline and highly uniform graphene layers derived from SiC nanowires are assembled in turbostratic layers within micron-thick fibers. Our simulations also confirm that the graphitic structures have been developed via a high temperature heat treatment of SiC. The mechanism driving this phenomenon can be described as a preferential evaporation of Si from the carbide that leaves behind a carbon skeleton, which subsequently graphitizes. At a first stage, the thermal energy injected into the system triggers the Si evaporation from the carbide. When most of the Si is gone, the thermal energy is employed into the atomic rearrangement of the amorphous carbon skeleton, thus yielding stacked graphene layers. We have also concluded that the formation of the novel compartmentalized/interconnected collapsed fiber structure is achieve through the temperature driven fast diffusion of Si and

the volume reduction of SiC structure. The facile graphene synthesis approach presented here opens up a new avenue towards cost-effective and etching-free free-standing graphene for bulk applications. With enhanced electrical conductivity and mechanical robustness from the high crystallinity, the self-standing graphene fiber could work as a platform to construct photovoltaic wire [58]. In addition, it can also be a promising candidate working as the current collector/anode for Na-ion battery with efficient ion and electron transport. When compared to the functionalized wood fibers, these graphene fibers with ~100 nm diameter derived from biomass, creates a multichannel and mesoporous structure with high electrical conductivity without the addition of other conducting materials [59].

**References**

[1]     K.S. Novoselov, A.K. Geim, S. V Morozov, D. Jiang, Y. Zhang, S. V Dubonos, et al., Electric field effect in atomically thin carbon films, Science. 306 (2004) 666–9. doi:10.1126/science.1102896.

[2]     K.S. Novoselov, V.I. Fal′ko, L. Colombo, P.R. Gellert, M.G. Schwab, K. Kim, A roadmap for graphene, Nature. 490 (2012) 192–200. doi:10.1038/nature11458.

[3]     Y. Hernandez, V. Nicolosi, M. Lotya, F.M. Blighe, Z. Sun, S. De, et al., High-yield production of graphene by liquid-phase exfoliation of graphite, Nat. Nanotechnol. 3 (2008) 563–568. doi:10.1038/nnano.2008.215.

[4]     S. Stankovich, D.A. Dikin, R.D. Piner, K.A. Kohlhaas, A. Kleinhammes, Y. Jia, et al., Synthesis of graphene-based nanosheets via chemical reduction of exfoliated graphite oxide, Carbon. 45 (2007) 1558–1565. doi:10.1016/j.carbon.2007.02.034.

[5]     X. Li, W. Cai, J. An, S. Kim, J. Nah, D. Yang, et al., Large-area synthesis of high-quality and uniform graphene films on copper foils, Science. 324 (2009) 1312–4. doi:10.1126/science.1171245.

[6]     S. Bae, H.R. Kim, Y. Lee, X. Xu, J.-S. Park, Y. Zheng, et al., Roll-to-roll production of 30-inch graphene films for transparent electrodes, Nat. Nanotechnol. 5 (2010) 574–578. doi:10.1038/nnano.2010.132.

[7]     C. Berger, Z. Song, X. Li, X. Wu, N. Brown, C. Naud, et al., Electronic confinement and coherence in patterned epitaxial graphene, Science. 312 (2006) 1191–6. doi:10.1126/science.1125925.

[8]     Y.-M. Lin, C. Dimitrakopoulos, K.A. Jenkins, D.B. Farmer, H.-Y. Chiu, A. Grill, et al., 100-GHz transistors from wafer-scale epitaxial graphene, Science. 327 (2010)

662. doi:10.1126/science.1184289.

[9]     A. Oberlin, M. Endo, T. Koyama, Filamentous growth of carbon through benzene

        decomposition, J. Cryst. Growth. 32 (1976) 335–349. doi:10.1016/0022-

        0248(76)90115-9.

[10]    M. Endo, Grow carbon fibers in the vapor phase, Chemtech. 18 (1988) 568–576.

[11]    F.C. Lanning, Plant constituents, silicon in rice, J. Agric. Food Chem. 11 (1963)

        435–437. doi:10.1021/jf60129a024.

[12]    D.S. Jung, M.-H. Ryou, Y.J. Sung, S. Bin Park, J.W. Choi, Recycling rice husks for

        high-capacity lithium battery anodes, Proc. Natl. Acad. Sci. U. S. A. 110 (2013)

        12229–34. doi:10.1073/pnas.1305025110.

[13]    L. Sun, K. Gong, Silicon-based materials from rice husks and their applications, Ind.

        Eng. Chem. Res. 40 (2001) 5861–5877. doi:10.1021/ie010284b.

[14]    V. Bansal, A. Ahmad, M. Sastry, Fungus-mediated biotransformation of amorphous

        silica in rice husk to nanocrystalline silica, J. Am. Chem. Soc. 128 (2006) 14059–66.

        doi:10.1021/ja062113+.

[15]    N. Liu, K. Huo, M.T. McDowell, J. Zhao, Y. Cui, Rice husks as a sustainable source

        of nanostructured silicon for high performance Li-ion battery anodes, Sci. Rep. 3

        (2013) 1919. doi:10.1038/srep01919.

[16]    S. Chandrasekhar, K.G. Satyanarayana, P.N. Pramada, P. Raghavan, T.N. Gupta,

        Processing, properties and applications of reactive silica from rice husk—an

        overview, J. Mater. Sci. 38 (2003) 3159–3168. doi:10.1023/A:1025157114800.

[17]    T.H. Liou, Preparation and characterization of nano-structured silica from rice husk,

Mater. Sci. Eng. A. 364 (2004) 313–323. doi:10.1016/j.msea.2003.08.045.

[18]  N.K. Sharma, W.S. Williams, A. Zangvil, Formation and structure of silicon carbide whiskers from rice hulls, J. Am. Ceram. Soc. 67 (1984) 715–720. doi:10.1111/j.1151-2916.1984.tb19507.x.

[19]  R.V. Krishnarao, Y.R. Mahajan, Formation of SiC whiskers from raw rice husks in argon atmosphere, Ceram. Int. 22 (1996) 353–358. doi:10.1016/0272-8842(95)00084-4.

[20]  R.V. Krishnarao, M.M. Godkhindi, P.G.I. Mukunda, M. Chakraborty, Direct pyrolysis of raw rice husks for maximization of silicon carbide whisker formation, J. Am. Ceram. Soc. 74 (1991) 2869–2875. doi:10.1111/j.1151-2916.1991.tb06856.x.

[21]  P.C. Silva, J.L. Figueiredo, Production of SiC and Si3N4 whiskers in C+SiO2 solid mixtures, Mater. Chem. Phys. 72 (2001) 326–331. doi:10.1016/S0254-0584(01)00332-7.

[22]  V. Pavarajarn, R. Precharyutasin, P. Praserthdam, Synthesis of silicon nitride fibers by the carbothermal reduction and nitridation of rice husk ash, J. Am. Ceram. Soc. 93 (2010) 973–979. doi:10.1111/j.1551-2916.2009.03530.x.

[23]  I.A. Rahman, Preparation of Si3N4 by carbothermal reduction of digested rice husk, Ceram. Int. 20 (1994) 195–199. doi:10.1016/0272-8842(94)90039-6.

[24]  G.T.-K. Fey, C.-L. Chen, High-capacity carbons for lithium-ion batteries prepared from rice husk, J. Power Sources. 97–98 (2001) 47–51. doi:10.1016/S0378-7753(01)00504-3.

[25]  E.Y.L. Teo, L. Muniandy, E.-P. Ng, F. Adam, A.R. Mohamed, R. Jose, et al., High

surface area activated carbon from rice husk as a high performance supercapacitor electrode, Electrochim. Acta. 192 (2016) 110–119. doi:10.1016/j.electacta.2016.01.140.

[26] Z. Wang, J. Yu, X. Zhang, N. Li, B. Liu, Y. Li, et al., Large-scale and controllable synthesis of graphene quantum dots from rice husk biomass: A comprehensive utilization strategy, ACS Appl. Mater. Interfaces. 8 (2016) 1434–9. doi:10.1021/acsami.5b10660.

[27] H. Muramatsu, Y.A. Kim, K.-S. Yang, R. Cruz-Silva, I. Toda, T. Yamada, et al., Rice husk-derived graphene with nano-sized domains and clean edges, Small. 10 (2014) 2766–70, 2740. doi:10.1002/smll.201400017.

[28] Z. Wang, H. Ogata, S. Morimoto, J. Ortiz-Medina, M. Fujishige, K. Takeuchi, et al., Nanocarbons from rice husk by microwave plasma irradiation: From graphene and carbon nanotubes to graphenated carbon nanotube hybrids, Carbon. 94 (2015) 479–484. doi:10.1016/j.carbon.2015.07.037.

[29] H. Katsuki, S. Furuta, T. Watari, S. Komarneni, ZSM-5 zeolite/porous carbon composite: Conventional- and microwave-hydrothermal synthesis from carbonized rice husk, Microporous Mesoporous Mater. 86 (2005) 145–151. doi:10.1016/j.micromeso.2005.07.010.

[30] A.K. Geim, K.S. Novoselov, The rise of graphene, Nat. Mater. 6 (2007) 183–91. doi:10.1038/nmat1849.

[31] S. Plimpton, Fast parallel algorithms for short-range molecular dynamics, J. Comput. Phys. 117 (1995) 1–19. doi:10.1006/jcph.1995.1039.

[32]    J. Tersoff, Modeling solid-state chemistry: Interatomic potentials for multicomponent systems, Phys. Rev. B. 39 (1989) 5566–5568. doi:10.1103/PhysRevB.39.5566.

[33]    H. Shen, MD simulations on the melting and compression of C, SiC and Si nanotubes, J. Mater. Sci. 42 (2007) 6382–6387. doi:10.1007/s10853-006-1205-2.

[34]    G. Bussi, D. Donadio, M. Parrinello, Canonical sampling through velocity rescaling, J. Chem. Phys. 126 (2007) 014101. doi:10.1063/1.2408420.

[35]    D.S. Franzblau, Computation of ring statistics for network models of solids, Phys. Rev. B. 44 (1991) 4925–4930. doi:10.1103/PhysRevB.44.4925.

[36]    C. Castiglioni, C. Mapelli, F. Negri, G. Zerbi, Origin of the D line in the Raman spectrum of graphite: A study based on Raman frequencies and intensities of polycyclic aromatic hydrocarbon molecules, J. Chem. Phys. 114 (2001) 963. doi:10.1063/1.1329670.

[37]    M.M. Lucchese, F. Stavale, E.H.M. Ferreira, C. Vilani, M.V.O. Moutinho, R.B. Capaz, et al., Quantifying ion-induced defects and Raman relaxation length in graphene, Carbon. 48 (2010) 1592–1597. doi:10.1016/j.carbon.2009.12.057.

[38]    A. Eckmann, A. Felten, A. Mishchenko, L. Britnell, R. Krupke, K.S. Novoselov, et al., Probing the nature of defects in graphene by Raman spectroscopy, Nano Lett. 12 (2012) 3925–30. doi:10.1021/nl300901a.

[39]    L. Lin, Synthesis and optical property of large-scale centimetres-long silicon carbide nanowires by catalyst-free CVD route under superatmospheric pressure conditions, Nanoscale. 3 (2011) 1582–91. doi:10.1039/c0nr00717j.

[40] S.B. Hanna, L.M. Farag, N.A.L. Mansour, Pyrolysis and combustion of treated and untreated rice hulls, Thermochim. Acta. 81 (1984) 77–86. doi:10.1016/0040-6031(84)85112-6.

[41] J. V. Milewski, F.D. Gac, J.J. Petrovic, S.R. Skaggs, Growth of beta-silicon carbide whiskers by the VLS process, J. Mater. Sci. 20 (1985) 1160–1166. doi:10.1007/BF01026309.

[42] F.J. Narciso-Romero, F. Rodríguez-Reinoso, Synthesis of SiC from rice husks catalysed by iron, cobalt or nickel, J. Mater. Sci. 31 (1996) 779–784. doi:10.1007/BF00367899.

[43] A.K. Ray, G. Mahanty, A. Ghose, Effect of catalysts and temperature on silicon carbide whiskers formation from rice husk, J. Mater. Sci. Lett. 10 (1991) 227–229. doi:10.1007/BF00723812.

[44] M.B. Vázquez-Santos, E. Geissler, K. László, J.-N. Rouzaud, A. Martínez-Alonso, J.M.D. Tascón, Comparative XRD, Raman, and TEM study on graphitization of PBO-derived carbon fibers, J. Phys. Chem. C. 116 (2012) 257–268. doi:10.1021/jp2084499.

[45] A.C. Ferrari, J.C. Meyer, V. Scardaci, C. Casiraghi, M. Lazzeri, F. Mauri, et al., Raman spectrum of graphene and graphene layers, Phys. Rev. Lett. 97 (2006) 187401. doi:10.1103/PhysRevLett.97.187401.

[46] C. Cong, T. Yu, R. Saito, G.F. Dresselhaus, M.S. Dresselhaus, Second-order overtone and combination Raman modes of graphene layers in the range of 1690-2150 cm-1, ACS Nano. 5 (2011) 1600–5. doi:10.1021/nn200010m.

[47]  R. Rao, R. Podila, R. Tsuchikawa, J. Katoch, D. Tishler, A.M. Rao, et al., Effects of layer stacking on the combination Raman modes in graphene, ACS Nano. 5 (2011) 1594–9. doi:10.1021/nn1031017.

[48]  D. Li, D. Zhan, J. Yan, C. Sun, Z. Li, Z. Ni, et al., Thickness and stacking geometry effects on high frequency overtone and combination Raman modes of graphene, J. Raman Spectrosc. 44 (2013) 86–91. doi:10.1002/jrs.4156.

[49]  U. Mogera, S. Walia, B. Bannur, M. Gedda, G.U. Kulkarni, Intrinsic nature of graphene revealed in temperature-dependent transport of twisted multilayer graphene, J. Phys. Chem. C. 121 (2017) 13938–13943. doi:10.1021/acs.jpcc.7b04068.

[50]  J. Campos-Delgado, L.G. Cançado, C.A. Achete, A. Jorio, J.-P. Raskin, Raman scattering study of the phonon dispersion in twisted bilayer graphene, Nano Res. 6 (2013) 269–274. doi:10.1007/s12274-013-0304-z.

[51]  R. He, T.-F. Chung, C. Delaney, C. Keiser, L.A. Jauregui, P.M. Shand, et al., Observation of low energy Raman modes in twisted bilayer graphene, Nano Lett. 13 (2013) 3594–601. doi:10.1021/nl4013387.

[52]  J. Hass, F. Varchon, J.E. Millán-Otoya, M. Sprinkle, N. Sharma, W.A. de Heer, et al., Why multilayer graphene on 4H−SiC(0001¯) behaves like a single sheet of graphene, Phys. Rev. Lett. 100 (2008) 125504. doi:10.1103/PhysRevLett.100.125504.

[53]  A. Oberlin, Carbonization and graphitization, Carbon. 22 (1984) 521–541. doi:10.1016/0008-6223(84)90086-1.

[54] M. Endo, Y.A. Kim, T. Hayashi, T. Yanagisawa, H. Muramatsu, M. Ezaka, et al., Microstructural changes induced in "stacked cup" carbon nanofibers by heat treatment, Carbon. 41 (2003) 1941–1947. doi:10.1016/S0008-6223(03)00171-4.

[55] L.G. Cançado, K. Takai, T. Enoki, M. Endo, Y.A. Kim, H. Mizusaki, et al., Measuring the degree of stacking order in graphite by Raman spectroscopy, Carbon. 46 (2008) 272–275. doi:10.1016/j.carbon.2007.11.015.

[56] W. Norimatsu, M. Kusunoki, Structural features of epitaxial graphene on SiC {0 0 0 1} surfaces, J. Phys. D. Appl. Phys. 47 (2014) 094017. doi:10.1088/0022-3727/47/9/094017.

[57] G.R. Yazdi, R. Vasiliauskas, T. Iakimov, A. Zakharov, M. Syväjärvi, R. Yakimova, Growth of large area monolayer graphene on 3C-SiC and a comparison with other SiC polytypes, Carbon. 57 (2013) 477–484. doi:10.1016/j.carbon.2013.02.022.

[58] Z. Yang, H. Sun, T. Chen, L. Qiu, Y. Luo, H. Peng, Photovoltaic wire derived from a graphene composite fiber achieving an 8.45 % energy conversion efficiency, Angew. Chem. Int. Ed. Engl. 52 (2013) 7545–8. doi:10.1002/anie.201301776.

[59] H. Zhu, Z. Jia, Y. Chen, N. Weadock, J. Wan, O. Vaaland, et al., Tin anode for sodium-ion batteries using natural wood fiber as a mechanical buffer and electrolyte reservoir, Nano Lett. 13 (2013) 3093–100. doi:10.1021/nl400998t.

# Supplementary Information

# For

# Facile 1D Graphene Fiber Synthesis from Agricultural By-product; A Silicon-mediated Graphenization Route

Kazunori Fujisawa[1,2,*], Yu Lei[2,3], Carla de Tomas[4], Irene Suarez-Martinez[4], Chanjing Zhou[2,3], Yu-Chuan Lin[2,3], Shruti Subramanian[2,3], Ana Laura Elías[1,2], Masatsugu Fujishige[5], Kenji Takeuchi[5], Joshua A. Robinson[2,3], Nigel Anthony Marks[4], Morinobu Endo[5], Mauricio Terrones[1,2,3,5,6,**]

[1] Department of Physics, The Pennsylvania State University, University Park, Pennsylvania 16802, USA

[2] Center for 2-Dimensional and Layered Materials, The Pennsylvania State University, University Park, Pennsylvania 16802, USA

[3] Department of Materials Science and Engineering, The Pennsylvania State University, University Park, Pennsylvania 16802, USA

[4] Department of Physics and Astronomy, Curtin University, Perth WA 6845, Australia

[5] Institute of Carbon Science and Technology, Shinshu University, 4-17-1 Wakasato, Nagano 380-8553, Japan

[6] Department of Chemistry, The Pennsylvania State University, University Park, Pennsylvania 16802, USA
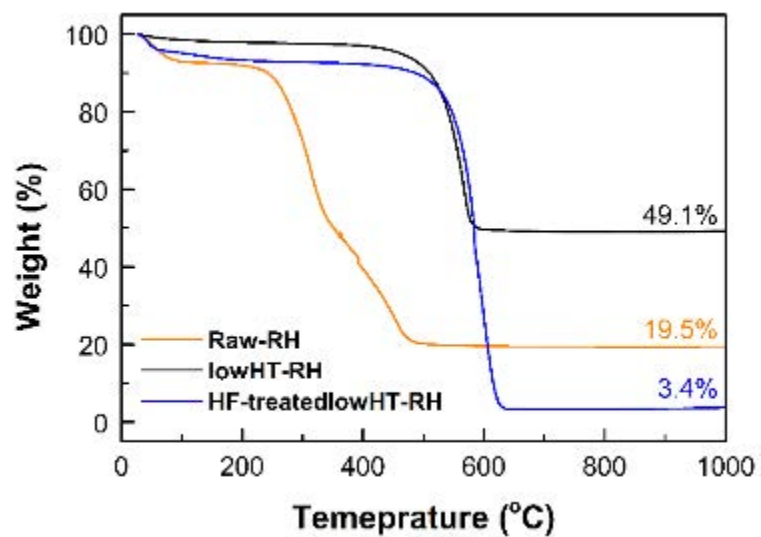
**Figure S1.** Thermogravimetric analysis of Raw-RH (orange), lowHT-RH (black) and HF-treated lowHT-RH (blue) carried out under 25 sccm of dry air flow.
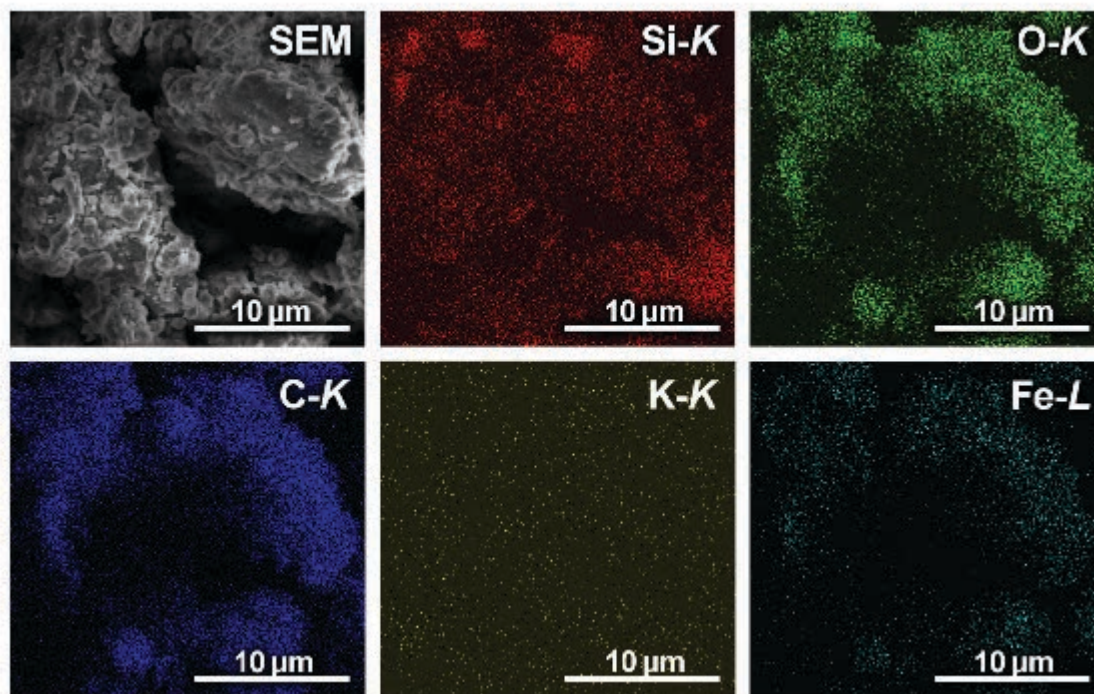
**Figure S2.** Energy dispersed X-ray mapping acquired from raw-RH sample.

**Table S1**. EDS-based elemental quantification acquired from raw-RH sample.

| Element | Line | Atomic % |
|---------|------|----------|
| C | K | 76.56 |
| O | K | 18.05 |
| Si | K | 4.03 |
| K | K | 0.13 |
| Ca | K | 0.07 |
| Cr | K | 0.12 |
| Fe | K | 1.03 |
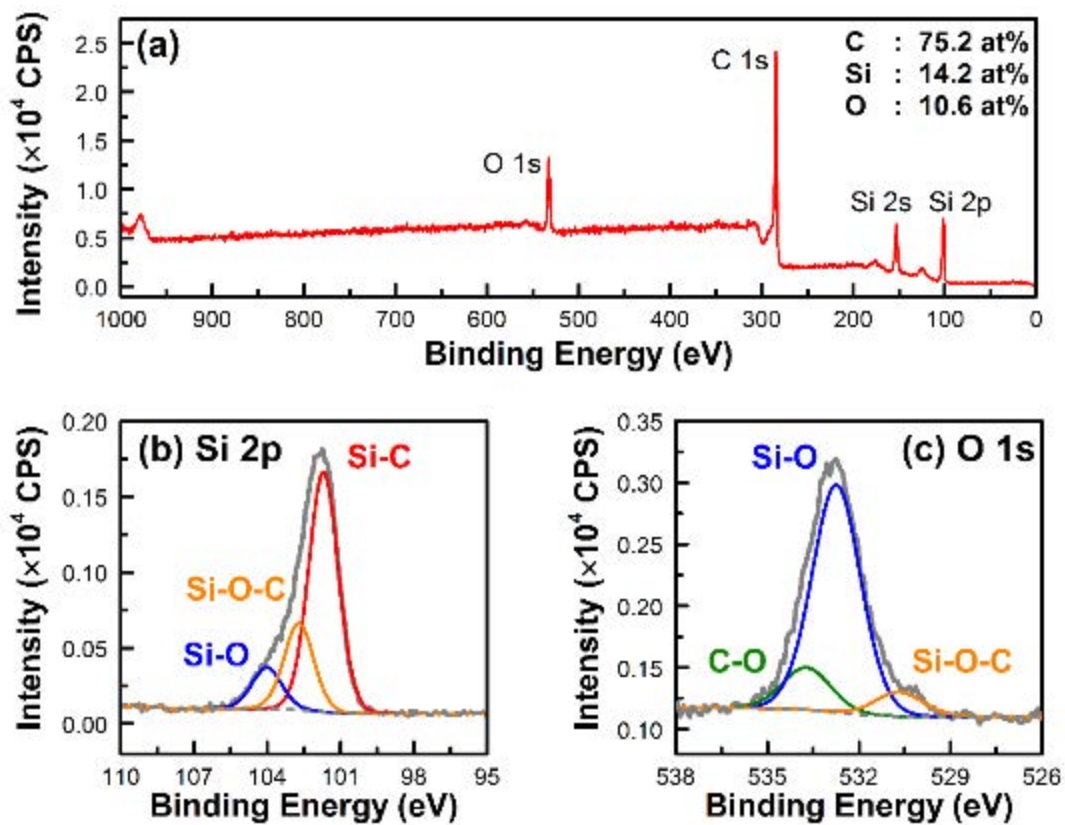
**Figure S3.** X-ray photoelectron spectra of midHT-RH sample; survey scan (a), high-resolution scan of Si 2p (b) and O 1s (c).
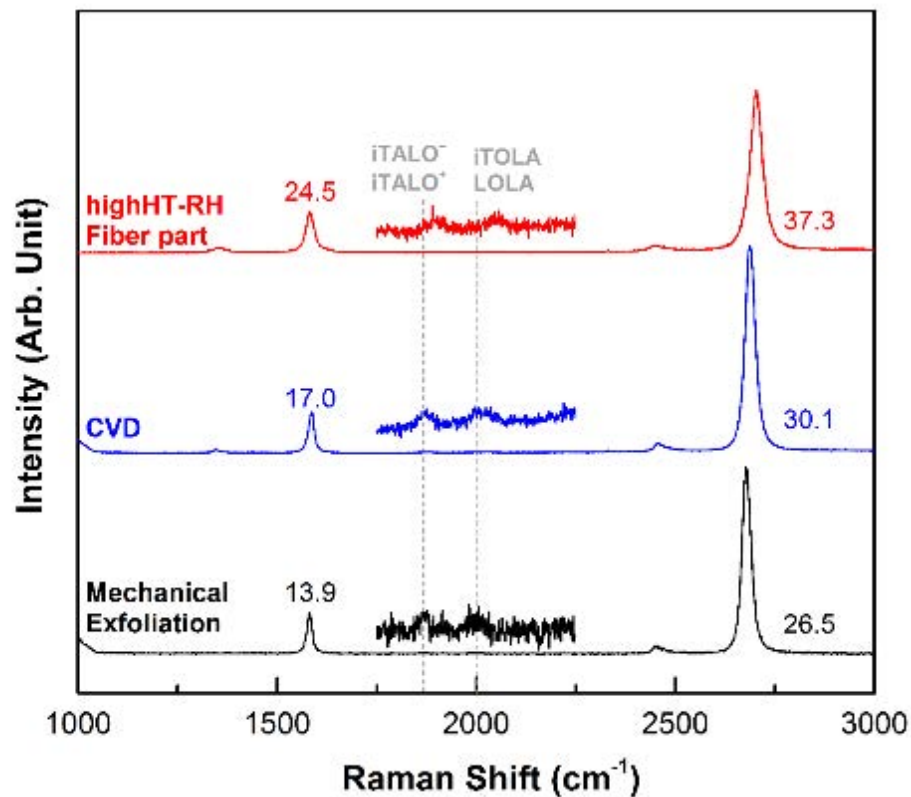
**Figure S4.** Comparison of Raman spectra collected from differently prepared graphene using 514.5 nm excitation. Two monolayer graphene samples on $SiO_2$/Si are prepared by methane-based CVD growth over copper substrate and mechanical exfoliation from graphite flake. The CVD-graphene was transferred onto $SiO_2$/Si substrate by polymer-assisted transfer technique. Full width at half maximum (FWHM) is denoted besides bands.
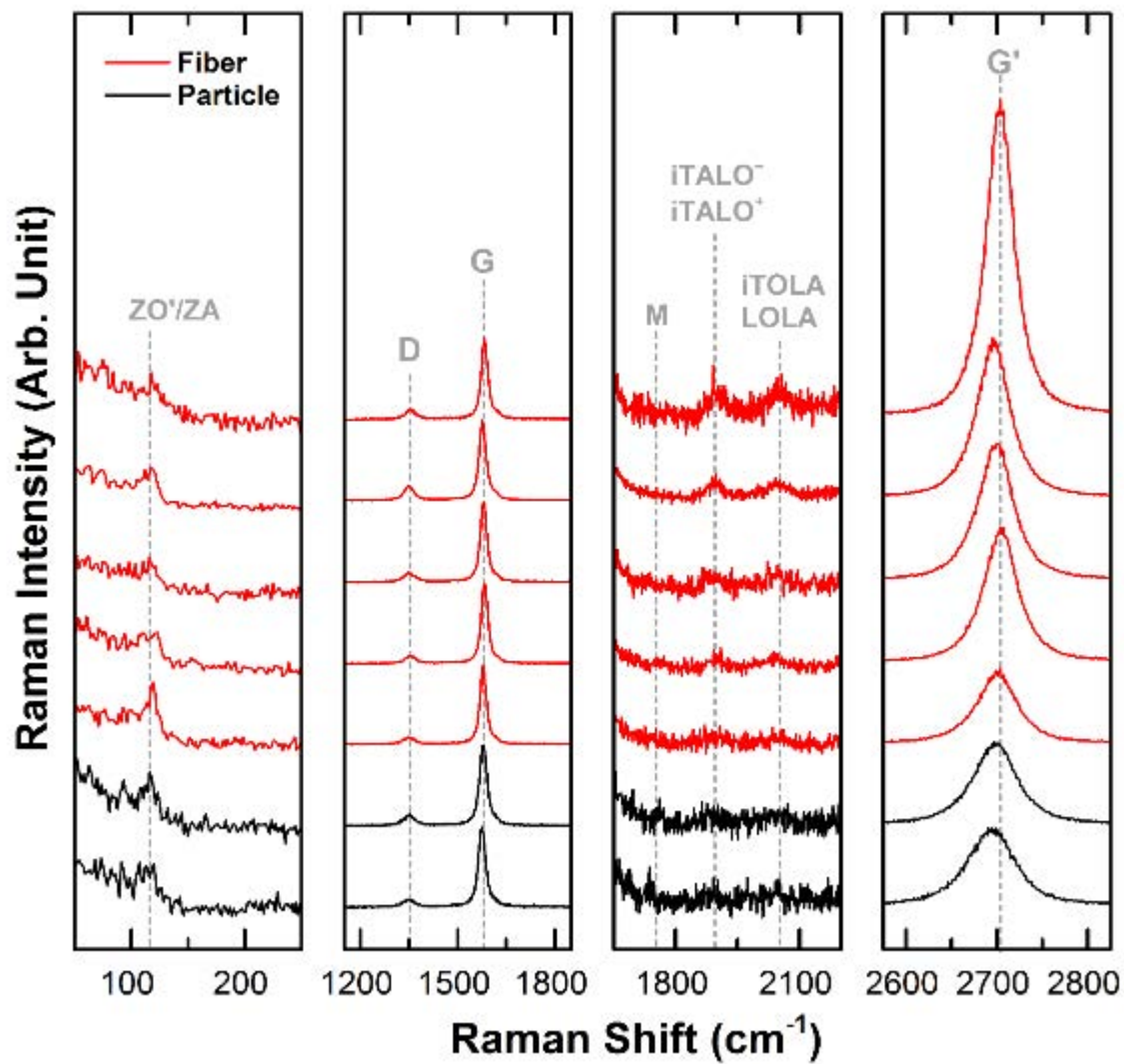
**Figure S5.** Detailed Raman profile acquired from the fiber and the particle part of highHT-RH sample using 514.5 nm excitation.
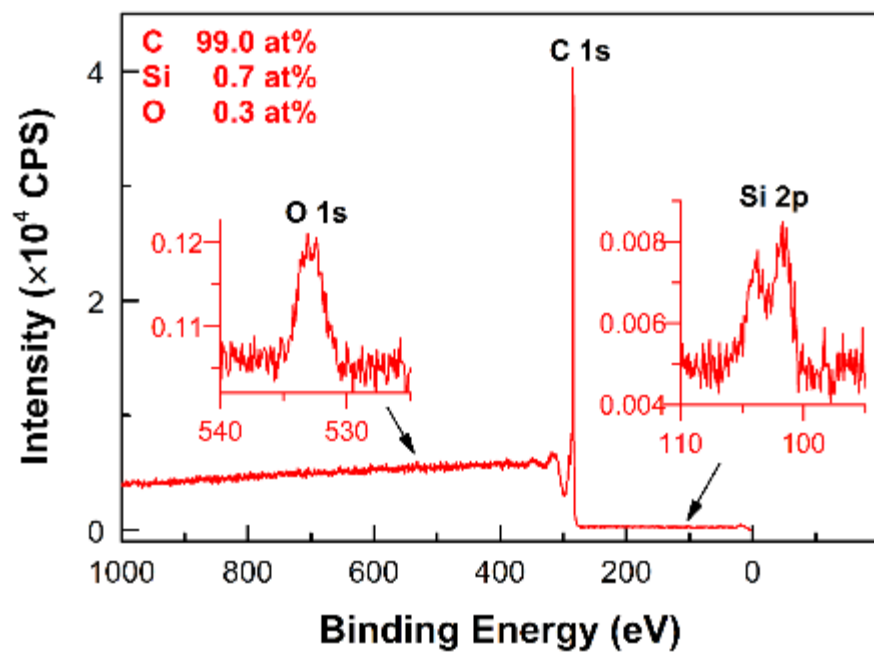
**Figure S6.** X-ray photoelectron spectrum acquired from highHT-RH sample.
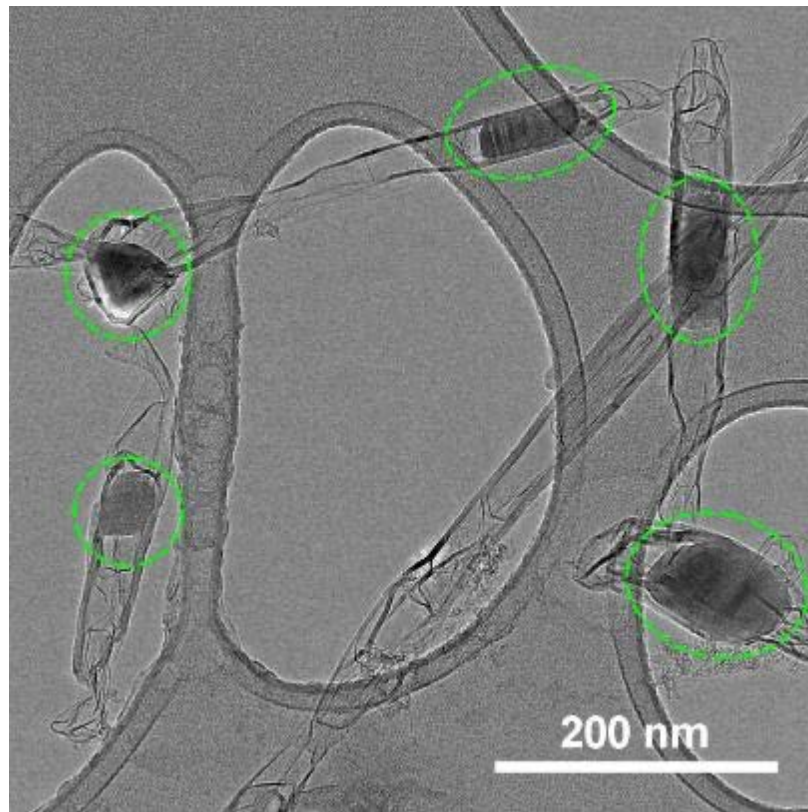
**Figure S7**. HRTEM image of highHT-RH sample. Remaining SiC structure after heat treatment is highlighted by circles.